Available online at www.sciencedirect.com
ScienceDirect
Acta Materialia 55 (2007) 3089–3102
Acta MATERIALIA
www.elsevier.com/locate/actamat

Evidence of variation in slip mode in a polycrystalline nickel-base superalloy with change in temperature from neutron diffraction strain measurements

M.R. Daymond [a,*], M. Preuss [b], B. Clausen [c]

[a] Department of Mechanical and Materials Engineering, Queen's University, Kingston, Canada K7L 3N6
[b] Manchester Materials Science Centre, University of Manchester, Manchester M1 7HS, UK
[c] LANSCE-12, Los Alamos National Laboratory, Los Alamos, NM 87545, USA

Received 6 October 2006; received in revised form 29 December 2006; accepted 4 January 2007
Available online 6 March 2007

Abstract

The deformation mechanisms under tensile loading in a 45 vol.% γ' polycrystalline nickel-base superalloy have been studied using neutron diffraction at 20 °C, 400 °C, 500 °C, 650 °C and 750 °C with the results interpreted via (self-consistent) polycrystal deformation modelling. The data demonstrate that such experiments are suited to detecting changes of the γ' slip mode from {111} to {100} with increasing temperature. Between room temperature and 500 °C there is load transfer from γ' to γ, indicating that γ' is the softer phase. At higher temperatures, opposite load transfer is observed indicating that the γ matrix is softer. At 400 °C and 500 °C, an instantaneous yielding increment of about 2% was observed, after an initial strain of 1.5%. This instantaneous straining coincided with zero lattice misfit between γ and γ' in the axial direction. Predicted and experimental results of the elastic strain response of the two phases and different grain families showed good agreement at elevated temperatures, while only qualitative agreement was found at 20 °C.
© 2007 Acta Materialia Inc. Published by Elsevier Ltd. All rights reserved.

Keywords: Diffraction; Superlattice; Internal strain; Self-consistent modelling

1. Introduction

Polycrystalline γ–γ' nickel-base superalloys represent an important class of two-phase materials with considerable technological interest because of their excellent high temperature properties, which arise from the presence of Ni_3Al (γ', $L1_2$-structure) precipitates embedded in the Ni alloy matrix (γ, fcc (face-centred cubic)). In order to increase the operating temperature in turbine engines, a new generation of nickel-base superalloys has been developed for disk applications containing a significantly higher volume fraction of γ' than previous superalloys. These new alloys have a γ' volume fraction of close to 50%. Understanding the deformation mechanisms is critical in these alloys, since it is necessary to ensure good tensile strength and fatigue properties alongside improved creep resistance.

In nickel-base superalloys, γ' precipitates are coherent with the γ matrix and display an exact cube–cube orientation relationship with the γ grains [1]. The unstressed lattice parameter of the γ' precipitates is generally slightly different to that of the γ matrix. The precipitation hardening mechanisms of γ'-strengthened nickel-base superalloys has been studied in great detail by a number of researchers [2–4]. It is now generally accepted that small γ' precipitates are cut by weakly and strongly paired dislocations and that large γ' precipitates are bypassed by Orowan looping. In the case of a duplex γ' distribution, it was shown empirically [5] that when the two classes of γ' precipitates exist as a randomly intermixed distribution, the individual yield

* Corresponding author. Tel.: +1 613 533 2193.
E-mail address: daymond@me.queensu.ca (M.R. Daymond).

1359-6454/$30.00 © 2007 Acta Materialia Inc. Published by Elsevier Ltd. All rights reserved.
doi:10.1016/j.actamat.2007.01.013

stress increments from these two mechanisms $\Delta\tau_1$ and $\Delta\tau_2$, superimpose to give a measured total yield stress increment $\Delta\tau_0$ described by

$$\Delta\tau_0^\alpha = \Delta\tau_1^\alpha + \Delta\tau_2^\alpha \quad (1)$$

For various combinations of strong γ' precipitates mixed among (shearable) weak precipitates, the superposition exponent α varies between 1 and 2 depending on the specific strength of the precipitates. In contrast, if there are well-defined regions of each class of γ' precipitate, a rule of mixture can be applied to give the total yield stress increment:

$$\Delta\tau_0 = A_1\Delta\tau_1 + A_2\Delta\tau_2 \quad (2)$$

where A_1 and A_2 are the area fractions.

In addition, it is well known that the $L1_2$ ordered structure displays an anomalous yield stress versus temperature behaviour, with Westbrook [6] first showing that Ni_3Al shows a peak hardness at elevated temperature. The most widely accepted mechanism for the flow stress increase was proposed by Thornton et al. [7] and involves cross slip of screw dislocations from (111) slip planes to the (010) planes where the dislocations are assumed to be immobile. This interaction can result in unusual behaviour where the high temperature (e.g. 550 °C) yield stress is higher than the room temperature value even though the strength of the γ phase decreases with increasing temperature. At even higher temperatures, diffusional mechanisms start to unlock the dislocations and the strength of γ' drops rapidly and with it the overall strength of the material. Therefore below the peak strength temperature, i.e. in the regime where the yield strength increases with rising temperature, the active slip systems are predominantly $\{111\}\langle 110\rangle$, while above the peak temperature $\{100\}\langle 110\rangle$ slip is predominant [8]. The driving force for the change of slip mode with increasing temperature is provided both by the anisotropy of the antiphase boundary (APB) and by the resolved shear stress on the $\{100\}\langle 110\rangle$ system. It was demonstrated by a number of researchers [9,10] that at high temperature, dislocations have a lower energy on the (010) plane than the (111) plane because the APB is at a minimum on the (010) plane. Further studies in this area showed that Shockley partials form during high temperature deformation, which cause the critical resolved shear stress (CRSS) of grains orientated near [001] and $[\bar{1}11]$ to be direction dependent [11,12]. To date, most of the experimental evidence of the change of the slip mode in γ' has been achieved by in situ transmission electron microscopy (TEM) studies on single crystal nickel-base superalloys [13]. However, if one wishes to study deformation mechanisms and micromechanics in polycrystalline nickel-base superalloys, such in situ TEM studies are far from ideal since the constraints imposed by the polycrystalline material do not exist in thin foil studies.

In this paper we report data obtained from in situ neutron diffraction studies carried out during tensile loading of Alloy 720Li, a γ'-strengthened alloy used by the aero-engine industry for disk applications. These measurements were undertaken between room temperature and 750 °C and explore the influence of the changes of slip mode on the distribution of internal interphase and intergranular strains. As will be discussed, clear qualitative and quantitative changes in behaviour can be seen as the testing temperature is raised. The interpretation of the experimental data is supported by a new two-site elastoplastic self-consistent (EPSC) polycrystal deformation model. The results demonstrate that the change of slip mode in γ' with increasing temperature in polycrystalline nickel-base superalloys can be detected by a combination of in situ neutron diffraction studies and EPSC modelling.

2. Experimental details

The material used in this study was Alloy 720Li, an advanced nickel-base superalloy containing about 45 vol.% γ' phase, a nominal value which was subsequently confirmed by analysis of the diffraction data. The material was produced by the cast and forged route and had an approximately random texture. The chemical composition of Alloy 720Li is given in Table 1. Since Al and Ti are strong γ' stabilisers and Ni can be substituted by Co [14], γ' in Alloy 720Li is best described as $(Ni,Co)_3(Al,Ti)$. The material was provided as a 150-mm cylinder by Rolls Royce plc and had been solution heat treated below the γ' solvus to avoid grain coarsening, followed by air cooling and a 16-h heat treatment at 760 °C. This heat treatment provides a material with a complex trimodal γ' distribution, which balances good strength and fatigue properties with sufficiently good creep resistance. The sub-solvus solution heat treatment resulted in coarse *inter*-granular γ', generally termed primary γ', shown in Fig. 1a. During cooling, *intra*-granular γ' starts to precipitate and coarsen, usually termed secondary γ'. As the material continues to cool, diffusion of γ' stabilising elements from the supersaturated matrix towards primary or secondary γ' becomes increasing difficult, resulting in the formation of fine, so-called tertiary γ' sitting between secondary γ' (Fig. 1b). The as-received material was first cut into slugs before machining into standard threaded tensile samples with a gauge diameter of 6 mm and gauge length of 40 mm.

Type I strains or stresses [15] can be determined by a range of methods, including diffraction-based, material removal and non-contact optical strain techniques. However, to determine the average phase elastic strain or the elastic strains in particular orientations of grains requires the use of diffraction methods. In typical neutron diffraction experiments, a gauge volume of several cubic millimetres is defined using apertures on the incident and diffracted beam paths, thus providing measurements of elastic strain typically averaged over several thousand grains. The method is well established and is described in, for example

Table 1
Nominal chemical composition of Alloy 720Li

Alloy	Cr	Co	Mo	W	Al	Ti	C	B	Ni
720 LI	18	15	3.0	1.25	2.5	5.0	0.020	0.032	Bal.

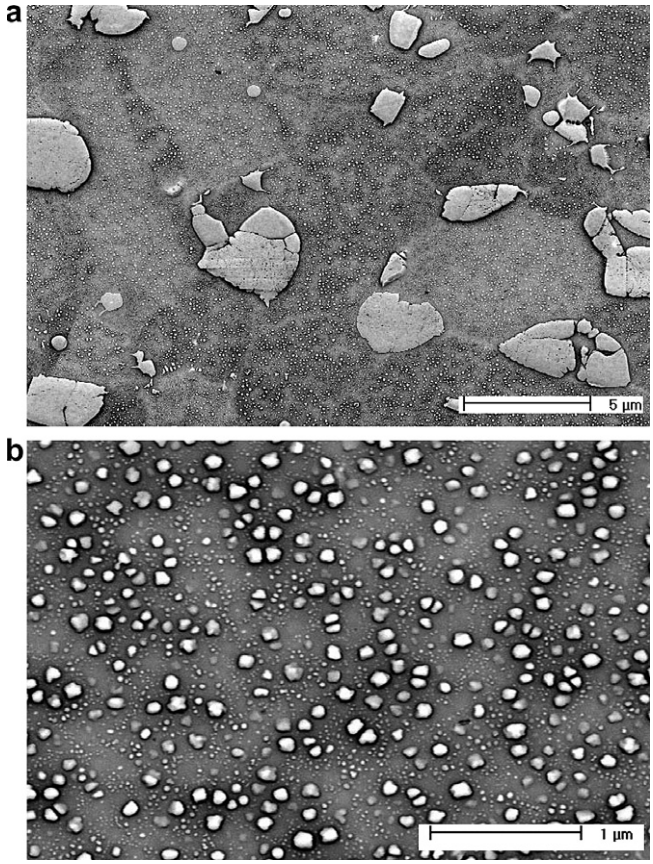

Fig. 1. Scanning electron microscopy images revealing (a) coarse intergranular primary γ' at low magnification and (b) intragranular secondary (coarse) and tertiary (fine) at high magnification in Alloy 720Li.

Refs. [16,17]. Here we emphasize however that such diffraction measurement involves monitoring of changes in separation of one or more suitably orientated crystallographic lattice planes. It is thus a direct measure of the elastic strain in the material. In a polycrystal, the lattice spacing obtained by fitting a diffraction peak represents the average lattice separation over all the grains in the irradiated volume which are suitably oriented to diffract.

A series of increasing uniaxial tensile loads were applied sequentially to each specimen in situ on the ENGIN-X instrument [18] at the ISIS pulsed neutron facility, Rutherford Appleton Laboratory. The load frame and its use is described in detail elsewhere [19], but in brief the loading axis is horizontal and at 45° to the incident beam, allowing simultaneous measurement of lattice plane spacing both parallel and perpendicular to the loading direction. The optical furnace used to heat the samples, in air, is described in more detail in Ref. [20]. The temperature was measured using a K-type thermocouple held in contact with the sample, just outside the neutron measurement volume. Measurements were carried out at temperatures of 20 °C, 400 °C, 500 °C, 650 °C and 750 °C.

At time-of-flight sources, such as ISIS, neutron pulses, each with a continuous range of velocities and therefore wavelengths, are directed at a specimen. The flight times of diffracted neutrons are measured, allowing calculation of wavelengths and the recording of diffraction spectra. The incident spectra are polychromatic, thus many lattice planes are recorded in each measurement. The scattering vectors for all reflections recorded in one detector lie in the same direction and thus indicate the strain in that direction in the sample. Each reflection is produced from a different family of grains, oriented such that a specific hkl plane diffracts to the detector. A more complete description of these issues can be found elsewhere [21]. It is now common practice at such a source to fit the whole spectrum simultaneously using a Rietveld refinement [22] when investigating the "average" or continuum equivalent strain in a phase. A two-phase Rietveld refinement was used to produce the phase average strains in each direction, parallel (longitudinal) and perpendicular (transverse) to the loading axis, respectively. Subsequently, to investigate how different grain orientations respond, we carried out fits to individual peaks within the spectrum, using the GSAS [23] software package, with an appropriate peak shape [24]. The diffraction data analysis in nickel-base superalloys is complicated by γ (fcc) and γ' ($L1_2$) exhibiting almost identical lattice parameters. Therefore any fundamental reflections observed during the experiment are produced from both phases. A method to deal with this was established for a low volume fraction γ' system and is described in detail in Ref. [25]. The method has also been used in the analysis of neutron diffraction studies of load sharing occurring in high γ' volume fraction systems [26,27]; the materials studied in these latter works had near cuboid γ' precipitates, in contrast to the microstructures seen here. In essence, the approach takes advantage of the fact that the γ' precipitates have an ordered structure primitive cubic lattice in which the nickel atoms are at the face centres and the aluminium or titanium atoms at the cube corners, while the γ grains are a solid solution with a fcc lattice and a random distribution of the different species of atoms. Since the γ' lattice is primitive cubic, additional superlattice reflections from the γ' precipitates are observed, which are weak since they depend on the difference in scattering power between the Ni and Al/Ti atoms. Thus the position of the first order γ' (e.g. 100, 110) peaks can be determined unambiguously. Using the known intensity relation based on the structure factor between first order γ' (100) and second order γ' (200), and the known d-spacing relation, it is

possible for the γ'–γ (200) doublet peak to be fitted using a constrained double peak fit. A similar approach is applicable to the analysis of the γ'–γ (220) peak. Peaks such as the (111) and (311) can only be analysed as a doublet since there is no lower order γ' peak available. Thus the only γ diffraction peaks for which strain can be determined are the (200) and (220) types, while this is possible for several γ' diffraction peaks. The doublet analysis was carried out using routines written in the OpenGenie software [28], again with the appropriate peak shape. As mentioned above, the two phases display a slight lattice mismatch which is known to contribute to the overall strength in single-crystal nickel-base superalloys [29]. However, in polycrystalline Ni superalloys, the influence of the γ/γ' lattice mismatch on mechanical properties is far less studied. As we measured the lattice spacing of each phase during the loading experiments, we report the evolution of the γ/γ' lattice mismatch during loading. In addition we report phase and grain specific strains and comparisons with model predictions. However, owing to restrictions in space available we are not able present all the data at all temperatures, and show in each case only key data sets that illustrate the transition in deformation mechanisms.

In interpreting the data reported in this paper, it should be pointed out that it is generally accepted that each type of γ' precipitate (primary, secondary and tertiary) has a different strengthening contribution to the overall mechanical properties of nickel-base superalloys. However, when recording the elastic strain from γ' superlattice peaks it is not possible to distinguish between these different types of γ' precipitates. As a consequence, the recorded elastic strain response of γ' has to be treated as an average of the complex γ' distribution. We aim to overcome this shortcoming in the future by generating uni-modal γ' distributions for such studies. This will be achieved by heat treating the material above the γ' transus followed by an oil quench, which suppresses any significant γ' coarsening during cooling. The model used to interpret the data has no intrinsic length scales in itself, thus any attempt to model the relative contribution of multiple types of γ' precipitate would be complex and will require interpretation of future experimental data obtained from uni-model distributions.

The tests were carried out under stress control and each neutron data acquisition (approximately 20 min) was then carried out at constant stress. This period of holding at constant stress provides time for a diffraction pattern of sufficient quality to be obtained. Macroscopic strain was monitored on the samples using a dynamic high temperature extensometer clip gauge in all cases. A slit 6 mm high and 4.5 mm wide defined the incident beam, while radial collimators provided a scattered beam width of 4.5 mm. In each case the strains shown are with respect to the initial lattice parameter measured at a nominal zero stress, for the given temperature. That is, strain $\varepsilon = (a - a_0)/a_0 = (d - d_0/d_0)$ where the lattice parameter a of each phase is determined by Rietveld refinement or the d-spacing of individual reflections from single peak fits, and a_0 and d_0 are the starting values. The strains reported thus do not show any contribution to the initial elastic strain from thermomechanical processing.

3. Description of model

To explore the different responses of the variously oriented grain families, i.e. to understand the behaviour of the individual diffraction peaks, we need to be able to describe the elastic–plastic properties of the polycrystalline aggregate. The response has been modelled here using a modification of the Hill self-consistent approach [30], first implemented by Hutchinson [31]. In this model a population of grains is chosen with a distribution of orientations and volume fractions that match the measured texture. Each grain in the model is treated as an ellipsoidal inclusion (here spherical) and is attributed anisotropic elastic constants and slip mechanisms characteristic of a single crystal of the material under study. Interactions between individual grains and the surrounding medium (which has properties of the average of all the grains) are performed using an elasto-plastic Eshelby-type self-consistent (EPSC) formulation [32]. Since the properties of the medium derive from the average response of all the grains, it is initially undetermined and must be solved by iteration. Small total deformations are assumed and no lattice rotation or texture development is incorporated. A single phase version of the model and its actual implementation are described in more detail in Ref. [33]. This model has been shown to be in good to excellent agreement in comparison with diffraction data for a range of materials, including fcc [34], bcc (body-centred cubic) [19] and hcp (hexagonal close packed) [35] crystal structures, and more recently multiphase systems [36,37] where there is no crystallographic relation between the two phases.

The extra complication present in the case of the Ni superalloy system is a well-defined crystallographic relationship between the γ matrix and the intragranular γ' precipitates. In order to model this, we have used a "two-site" modification of the Hill self-consistent formulation. In this case, two ellipsoids are modelled within the medium. The Eshelby tensor becomes roughly four times as complicated as in the one-site case because of the requirement for interaction between the ellipsoids. The approach used in the implementation of the model is similar to the one used by Lebensohn and Canova [38] for a two-site large strain visco-plastic self-consistent (VPSC) model, but here modified for elasto-plastic conditions [39]. The principal equations are given in Appendix 1. For the Ni superalloy system, each "grain" is then modelled as a γ ellipsoid in contact with a γ' ellipsoid. Each ellipsoid has the same crystallographic orientation but is given appropriate phase properties. The ellipsoid doublet then must deform as a unit within the medium. This is an approximation to the embedded structure seen in Fig. 1.

The single crystal elastic constants used in the model were determined from fitting to the experimental data reported in Ref. [40] for pure Ni_3Al as a function of temperature. Given the alloying elements present in Alloy 720Li, this must be an approximation and indeed the predicted macroscopic moduli based on these values were found to be uniformly too low. Following the approach in Ref. [41], the single crystal constants were increased by the same fraction (i.e. maintaining the same elastic anisotropy) in order to match the observed macroscopic moduli (Table 2). This required an increase of between 8% for the 750 °C data to 11% for the room temperature data. Again, without better data available, the same single crystal constants are used for the γ' and γ phases. This should be a reasonable approximation, since the differences are expected to be small [42]. While the use of such constants thus clearly represents a considerable assumption and a potential cause for error, the good agreement obtained between model and experiment, as reported in the next section, gives strong support for the approach used.

For the plastic flow law for a given slip system, the critical resolved shear stress and exponential hardening coefficients are typically used as fitting parameters. The hardening function used for each system is described by (3) [43],

$$\tau = \tau_0 + (\tau_1 + \theta_1 \Gamma)\left(1 - \exp\left[\frac{\theta_0 \Gamma}{\tau_1}\right]\right) \quad (3)$$

where Γ is the accumulated shear strain in the grain. The crystallographic shear flow stress τ in Eq. (3) describes (in an average way) the resistance to activation that the deformation modes experience. The threshold value is τ_0, and it usually increases with deformation caused by strain hardening, which is here assumed to follow a modified Voce law [43]; τ_1 is the Voce stress where the hardening extrapolates to a zero value of accumulated shear and θ_0 is the athermal initial hardening rate [43,44], while the Voce law has also been extended [43] to allow for an asymptotic hardening rate of θ_1.

Plastic slip in the γ phase was assumed to take place on the twenty-four $\langle 1\,1\,0\rangle\{1\,1\,1\}$ systems. At room temperature, this slip system was also assumed for the γ' phase while at 750 °C, slip in the γ' phase was assumed to take place on just $\langle 1\,1\,0\rangle\{1\,0\,0\}$ [7]. At intermediate temperatures, both slip systems were included for the γ' phase. The critical resolved shear stress, the Voce stress and hardening coefficients were used as fitting parameters. These were chosen so as to produce an optimum fit with the measured macroscopic stress strain curves and the average phase strains observed by diffraction. The same set of yield and hardening values are initially applied to all systems and grains (i.e. there are four parameters in the model for each type of slip system, for a given test). Each individual slip system on that type in a given grain is subsequently kept track of during modelling of the deformation and the hardening curve followed appropriately according to the accumulated shear strain. An isotropic hardening model was used, i.e. with latent hardening equal to self-hardening.

Table 2
Elastic constants used in the plasticity model for γ and γ'

Temperature/°C	C_{11}/GPa	C_{12}/GPa	C_{44}/GPa
20	254.6	170.9	137.4
400	242.6	168.7	125.1
500	238.9	167.5	121.7
650	227.0	161.2	113.2
750	223.1	160.1	109.6

We note that an alternative approach to modelling the γ–γ' system using a modification of the EPSC model was taken by Dye et al. [42]. There are some fundamental differences between that approach and the one taken here. First, the earlier work considers only room temperature data for a low volume fraction (15% γ') traditional superalloy and the γ' phase is treated as always remaining elastic. Secondly, the secondary precipitate phase is embedded within the primary phase using a second separate Eshelby calculation; it is thus a modification of the one-site approach. In fact, this actually leads to a contradiction, since one of the requirements/conclusions of the Eshelby solution is that the stress field inside the ellipse is uniform. It is likely that this may contribute to the reason that Dye's calculations were so computationally demanding.

In order to provide reasonable comparisons with diffraction data, a subset of the total population of grains used in the model is identified for each diffracting family, defined by the condition of having an hkl plane-normal lying within a 5° cone around the nominal scattering direction. A random texture was used, with 1000 grain "doublets" to represent the material and a 45% weighting for the γ' phase (55% for the γ phase) to match the phase volume fractions.

4. Results and discussion

The macroscopic stress–strain curves obtained during the neutron tests are shown in Fig. 2. Significant differences can be seen as a function of temperature. First, there is a slight reduction in the observed Young's modulus as the temperature is raised. More importantly there is a significant initial increase in yield stress as the temperature is raised from 20 °C to 400 °C and a smaller further increase in yield stress upon increasing to 500 °C. In addition, the shape of the stress–strain curve, i.e. the development of hardening, changes. At 20 °C, yielding is relatively sharp, with a then more or less constant hardening slope (over the strain range shown). At 400 °C and 500 °C, the initial yielding is more gradual, and the steady state hardening is of a lower gradient than that seen at 20 °C. Upon further increase in temperature, there is a drastic drop in the yield stress as 650 °C is reached, and then again a smaller further drop on going from 650 °C to 750 °C. The hardening response at 650 °C is in fact comparable to that seen at

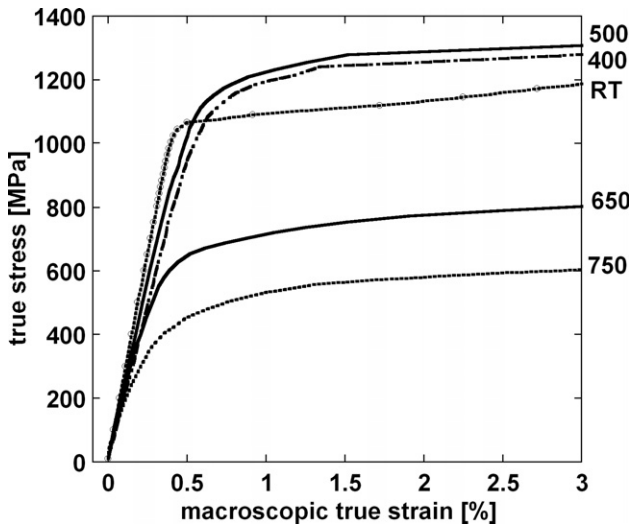

Fig. 2. Experimental macroscopic stress–strain response recorded during the loading experiments on ENGIN-X.

500 °C, while that at 750 °C is even more gradual. The peak in strength for this alloy is observed at a somewhat lower temperature than the temperatures typically reported for maximum critical resolved shear stress for the nickel superalloys used in single crystal applications, as reviewed in Ref. [45].

4.1. Average phase elastic strains

Fig. 3a–e shows the average phase strains as determined by changes in the lattice parameter obtained from the Rietveld refinement, in the direction parallel and perpendicular to the applied load in the tests. The strain obtained in this way is a good approximation to the average elastic strain in the phase, both in cubic [46] and lower symmetry [47] crystal structures. First, we note that the elastic moduli of the two phases measured in the longitudinal direction are in agreement with the accuracy of the observed experimental data; only at room temperature do the data support a slightly different modulus. Thus this represents a composite where there is relatively little load sharing in the elastic regime – analogous to the case of ferrite–cementite [48] or Ti–SiC composites [49]. The elastic slope in the transverse direction is in all cases roughly 0.3 of that observed in the axial direction and represents Poisson contraction.

The observation of plastic behaviour in the macroscopic stress–strain curve (Fig. 2) correlates with the observation of inflections in the average phase strains in Fig. 3, that is load transfer between phases becomes significant once plasticity occurs. Let us consider the data at 400 °C (Fig. 3b) and apply simple composite load transfer arguments. The γ' phase initially yields at an applied stress of around 1000 MPa and, for a given increment of stress, bears a smaller increment in elastic strain than in the elastic region. This is seen in the longitudinal and transverse directions. Correspondingly, the γ phase

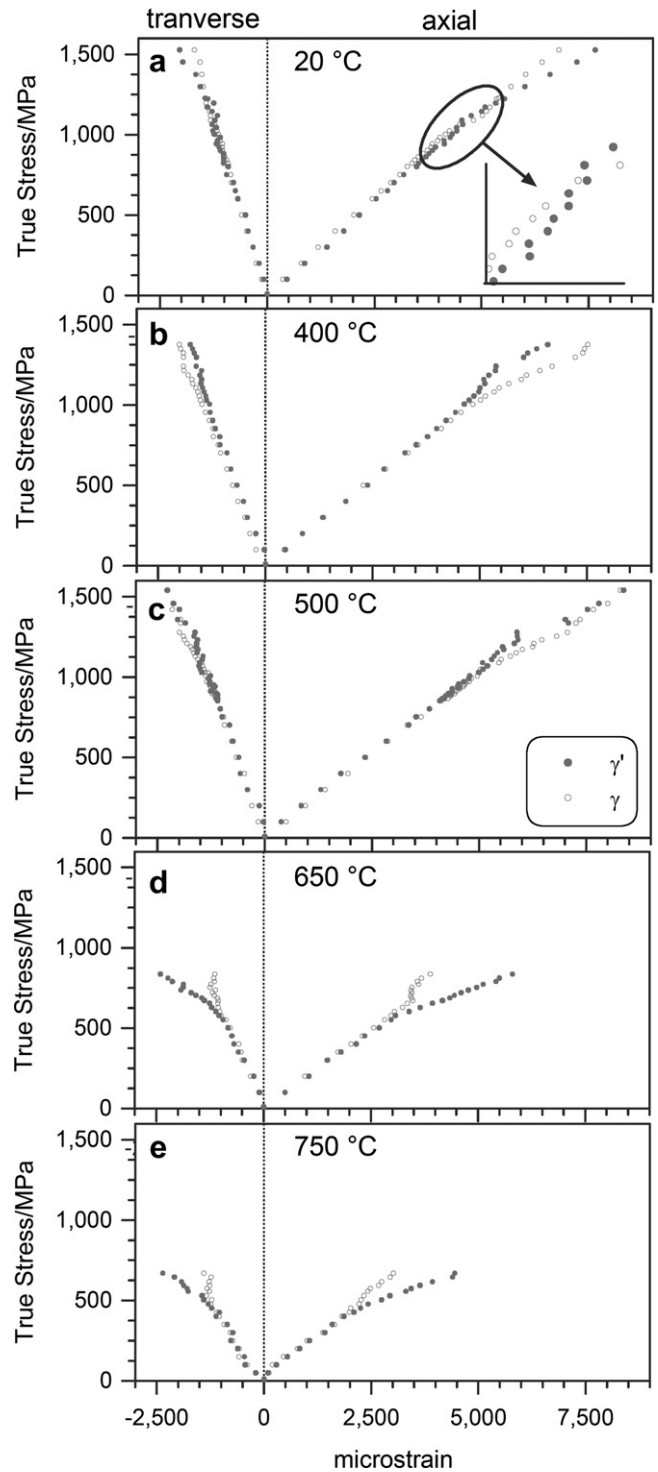

Fig. 3. Axial and transverse elastic strain response of γ and γ' during loading at (a) 20 °C, (b) 400 °C, (c) 500 °C, (d) 650 °C and (e) 750 °C.

bears a larger increment of elastic strain, i.e. there is load transfer from γ' to γ. It is perhaps surprising that at 400 °C the γ' phase seems to yield plastically before the γ phase. As further plasticity occurs, the slope of the γ' response in the longitudinal direction curves to the right (in the transverse direction to the left), as the material again bears a larger strain increment. This presumably

corresponds to hardening of the γ' phase and yield of the γ phase. At 500 °C, higher applied stresses were achieved and with it the effect of γ' hardening and the reversal in load transfer is more significant than at 400 °C, with the phase strains actually crossing over. That is, while at lower plastic strains/applied stresses, the 400 °C and 500 °C phase strains show similar behaviour (the γ' phase bearing less load); as plasticity progresses at 500 °C, the hardening of the γ' phase results in a reverse of the load transfer with the γ' phase carrying more load than the γ phase for very large plastic strains/applied stresses. It is interesting that at room temperature, a very similar effect to that seen at 500 °C is observed, with an initial γ' yield, but subsequent reversal of the load transfer resulting in two crossovers of the γ–γ' phase strain curves. However at room temperature the level of the initial load transfer (see also insert in Fig. 3a) is much smaller than that seen at 500 °C, indicating that γ' hardening happens more quickly at room temperature compared to 400 °C and 500 °C. The reasons for this rapid hardening are not clear, but it is perhaps due to the highly constrained microstructure of the γ' phase combined with a limited number of potential slip systems, with only the $\langle 110 \rangle \{111\}$ operating at this temperature. The data certainly demonstrate that an assumption of purely elastic response of γ' at room temperature, as in Ref. [42], is not correct in our case. As the temperature is raised to 650 °C, a clear change in qualitative response occurs, with the γ phase yielding first and showing a vertical elastic strain–stress response in both longitudinal and transverse directions. As plasticity occurs, there is yielding in the γ' phase evidenced by a change in curvature. The relative magnitude of the plastic misfit strains in the transverse direction seen at the different temperatures are approximately half the magnitude of the plastic misfit strains seen in the longitudinal direction demonstrating a Poisson effect, with the Poisson's ratio now increased owing to plastic flow.

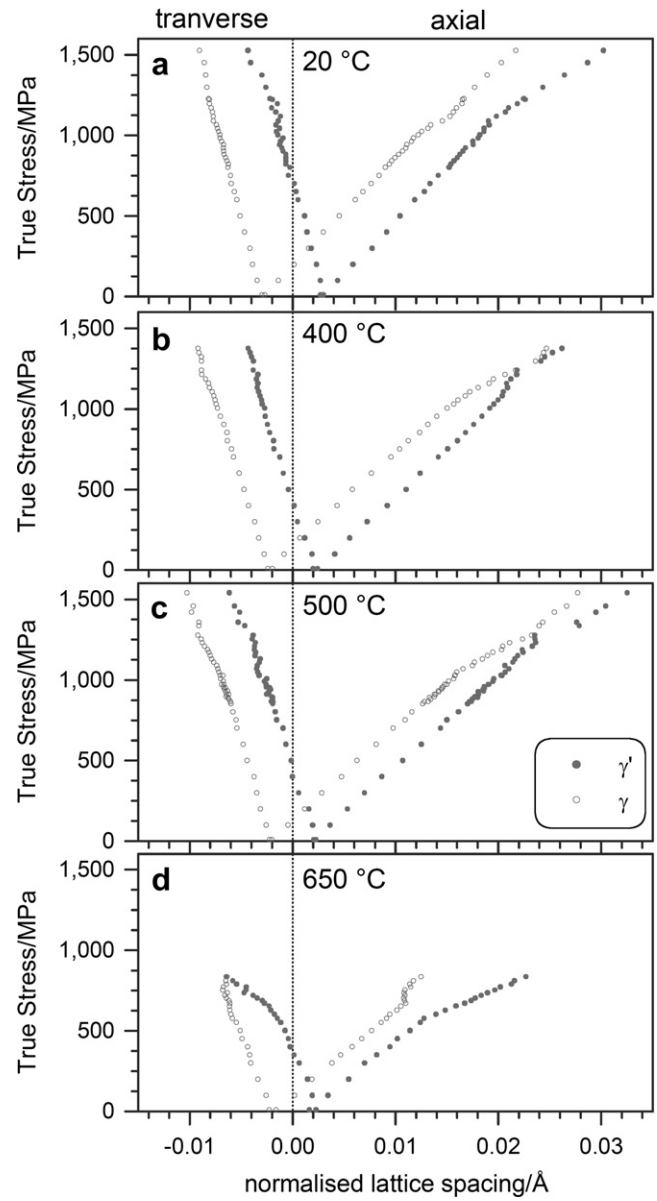

Fig. 4. Axial and transverse *d*-spacing response of γ and γ' during loading at (a) 20 °C, (b) 400 °C, (c) 500 °C, (d) 650 °C.

4.2. Average phase d-spacing

Since the intragranular γ' is coherent in the γ matrix, any load transfer between the two phases leads to a change of elastic misfit between γ and γ'. Fig. 4 shows the *d*-spacings corresponding to the strains reported in Fig. 3. The linear elastic regions and inflections associated with plasticity can be clearly seen. The initial misfit seen between the lattice parameter of the two phases corresponds to a coherency strain of about 0.16% (1600 microstrain) in the longitudinal and transverse directions at room temperature. With increasing temperature this initial coherency strain becomes smaller and reaches a value of about 0.06% in the axial and 0.09% in the transverse direction at 750 °C (data not shown, for reasons of space).

As discussed above, when loading between room temperature and 500 °C, at the onset of plastic yielding the load is transferred from γ' towards γ. As a result, at the onset of plastic yielding, the misfit between the two phases decreases in the longitudinal and increases in the transverse direction, as can be seen in Fig. 4a–d. In contrast, when the material was loaded at 650 °C (and 750 °C, not shown), at the onset of plastic yielding opposite load transfer between the two phases is observed and consequently, the axial misfit increases while the transverse misfit decreases (see Fig. 4d). A more quantitative evaluation is given in Fig. 5a–d, plotting the longitudinal and transverse coherency strain against macroscopic plastic true strain. It is interesting to note that at 400 °C and 500 °C, after straining the samples to about 1.5% (at ~1250 MPa) and the axial coherency strains had reached a value of zero, a large instantaneous plastic deformation of about 2% occurred (deformation happened in less than a second). The instantaneous

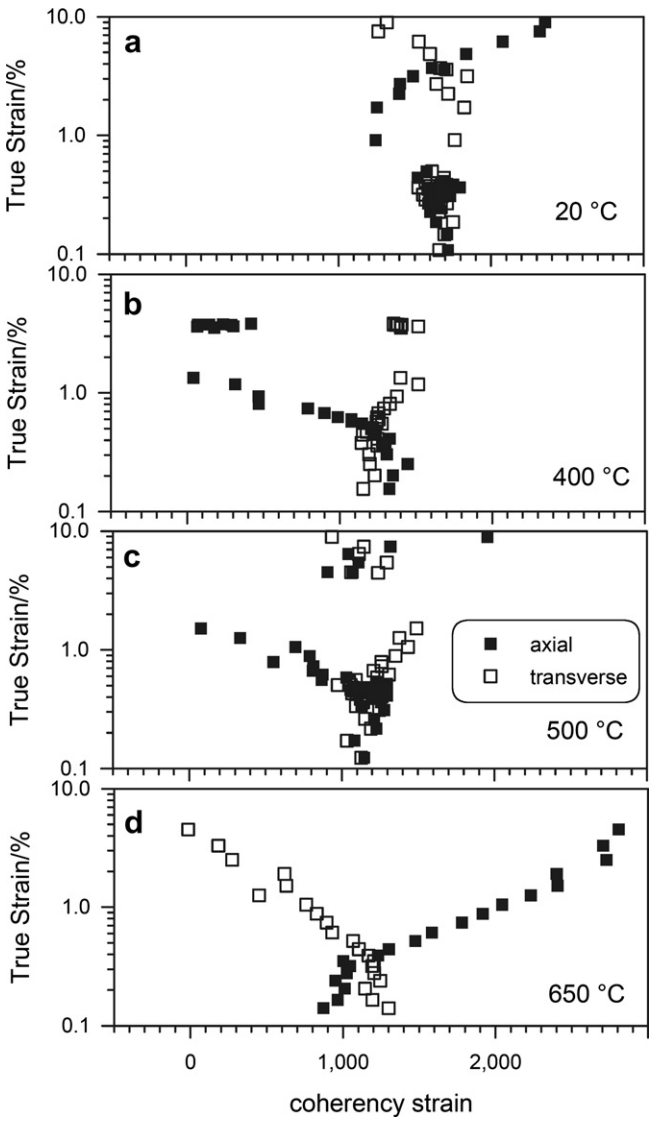

Fig. 5. Axial and transverse coherency strain against macroscopic plastic true strain at (a) 20 °C, (b) 400 °C, (c) 500 °C, (d) 650 °C.

deformation resulted in a dramatic reduction in the difference between axial and transverse coherency strain. It can be also seen in Fig. 3b and c that the instantaneous deformation led to significant γ' hardening, indicated by a jump in the measured elastic strain of almost 1000 microstrain. As the elastic misfit between γ and γ' has an impact on the energy necessary to transfer dislocations between the two phases, we suggest that the significant plastic deformation observed during tensile loading at this particular moment may be related to the zero longitudinal γ/γ' misfit. Fig. 5d shows that at 650 °C (similarly for 750 °C, not shown) the transverse coherency strain reaches zero when the material was strained in excess of 4% at 650 °C (9% at 750 °C). At the same time, the axial coherency strain reached large values, between 2000 and 3000 microstrain. No instantaneous straining was observed at this stage, which is most likely due to the large plastic strains already experienced by both phases.

4.3. Single peak strains

Plots of individual peak strains have been studied in detail in conventional fcc materials and information regarding the slip mechanisms can be extracted (see for example Ref. [34]). We summarise the key observations from such work to help with the interpretation of the data shown. The response of each peak is approximately linear in the macroscopically elastic regime, with a gradient dependent on the elastic anisotropy. Deviations from the elastic linear response occur close to the onset of macroscopic plasticity, but at different macroscopic applied stresses for different grain populations and in different senses. Certain grains are preferentially oriented for slip relative to their neighbours. In the case of materials with low elastic anisotropy (e.g. aluminium alloys), this is understood based on the Schmid factor of the particular crystallite orientation. Added complexity is introduced once elastic anisotropy is taken into account, since this results in different grains experiencing significantly different stresses and hence a more complex yield response. Based on composite mechanics arguments, these yielding grains then take up a relatively smaller increment in elastic strain than in the elastic regime, i.e. curving upwards into compression relative to the elastic line.

There is additional complexity in our case, because of the load transfer between phases, with the load transfer between grain orientations superimposed on top of this. The strains observed experimentally in the "doublet" peaks, (220) and (200), where the response of both γ and γ' grain families can be determined, are shown in Fig. 6a–d. The strain reported for each peak represents the average strain response of the subset of grains for that phase oriented for diffraction. In the following discussion, the term "grain family" refers to the subset of grains which contribute to a particular diffraction reflection along a certain scattering direction. That is, the longitudinal hkl grain family comprises all grains in which an {hkl} plane normal lies parallel to or within a few degrees of the tensile axis.

The 400 °C and 650 °C data sets show qualitatively similar responses to those seen in phase average strains, Fig. 3. The 750 °C data set is very similar to the 650 °C data set and is not shown for space reasons. Thus at 400 °C the γ' phase is plastically softer, whilst at 650 °C the γ phase is plastically softer. Interestingly, at 500 °C, we have reached a point in transition between these behaviours. Thus the γ phase shows a larger strain than the γ' phase in the (100) type peaks, as seen at 400 °C, but the opposite relationship is seen for the (110) type peaks – as seen at 650 °C. It is tempting to assume this shows a shift in mechanism, but it is also possible that at 500 °C we have simply reached a balance where the magnitude of the interphase load transfer is of comparable magnitude to that caused by intergranular load transfer. At 20 °C, the double crossovers seen in the mean phase strains cannot be resolved

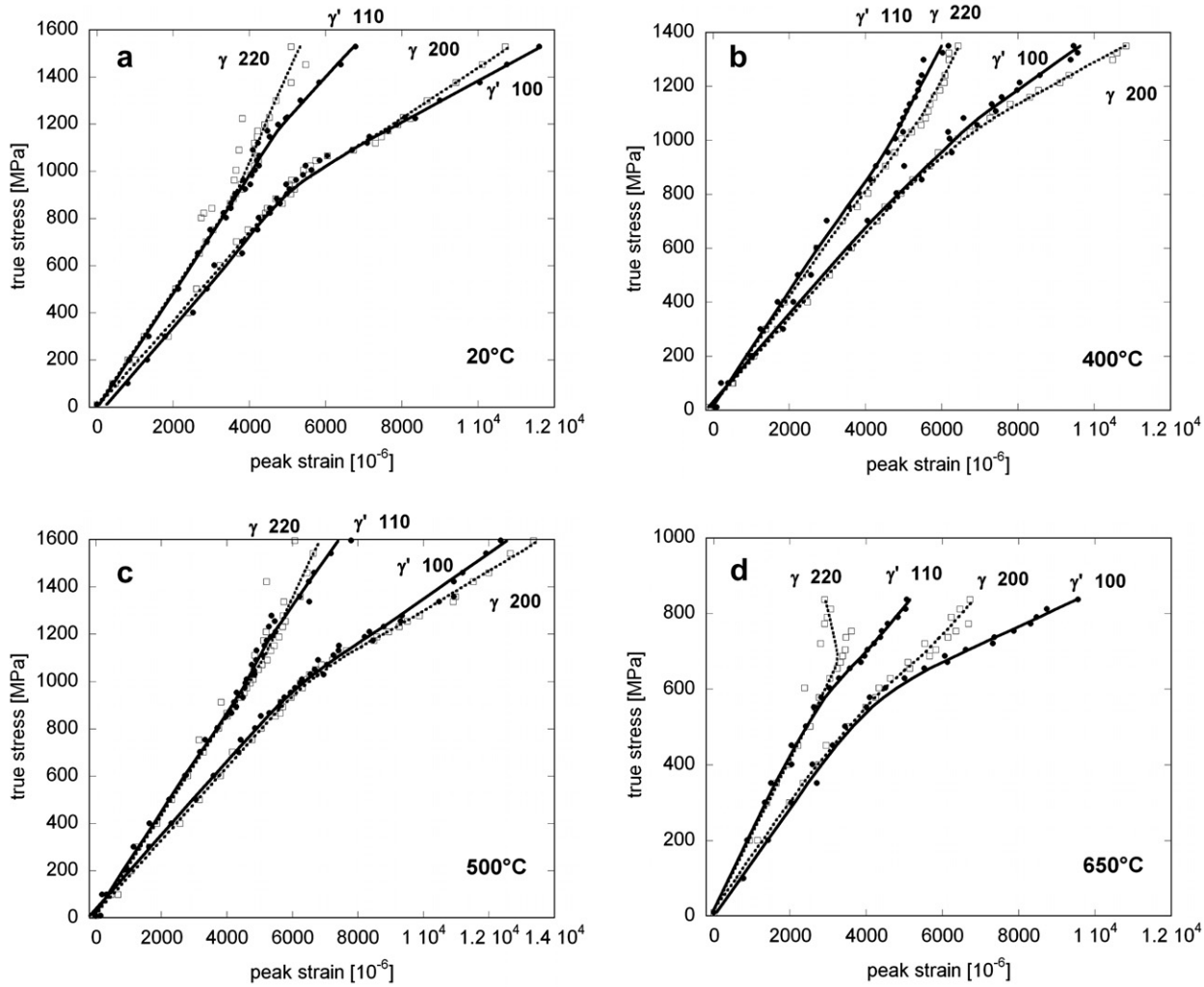

Fig. 6. Axial strain response of the (100) and (110) γ' reflections and the (200) and (220) γ reflections during tensile loading. The experimental data are plotted for measurements undertaken at (a) 20 °C, (b) 400 °C, (c) 500 °C, (d) 650 °C. The lines represent "best fit" to the data and are a guide to the eye.

owing to the higher statistical uncertainty in the single peak strains. Finally, we note that at 650 °C (and 750 °C) the differences between the strains observed in the two phases are significantly larger than in any of the other plots.

4.4. CRSS obtained from EPSC modelling

As discussed earlier, an optimum agreement between the plasticity model and the macroscopic stress–strain curves was achieved by considering the plastic flow law and a fitting approach to identify the CRSS and exponential hardening coefficients for each phase, for the temperatures tested. Fig. 7 displays the CRSS data for slip on the {111} slip planes in γ and γ' and the {100} slip planes in γ' as a function of temperature, which provided the best fit simultaneously between the experimental and predicted stress–strain curves, and the phase average stresses. As one would perhaps expect, the CRSS in γ' first increases between room temperature and 500 °C

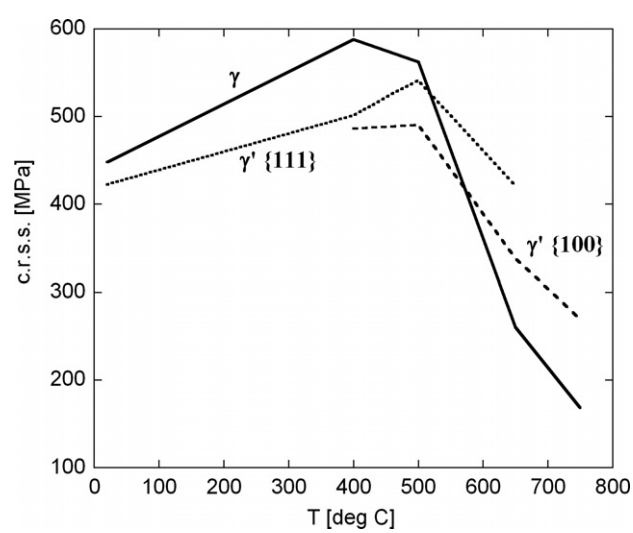

Fig. 7. CRSS values used in the plasticity model as a function of temperature, which provided the best fit between the predicted and experimentally measured stress–strain curves.

before it decreases between 500 °C and 750 °C. At 400 °C the CRSS of γ' for slip on {100} is slightly lower than on {111}. This tendency increases with rising temperature. As one would expect from the experimental data, the CRSS of γ for slip on {111} stays above the CRSS of γ' up to a temperature of 500 °C. Beyond this temperature the CRSS of γ drops more rapidly than that of the γ' phase, which results in CRSS values smaller for γ than γ'. The temperature dependency of the CRSS values for the γ matrix seen in Fig. 7 is as expected for the high temperature region. However, at room temperature, the model suggests a lower CRSS than at 400 °C. This result is clearly unexpected since the fcc structure of the γ matrix should not display any strengthening anomaly and highlights the limitations of the two-phase EPSC model applied in this study. It is interesting to note however that the model does not seem to capture the behaviour of the mean phase strains observed at room temperature as well as it does at elevated temperatures, as discussed in the next section. It should be noted that this is the only model run where the model does not incorporate {100} slip in the γ' phase. Hence one explanation is that perhaps the model cannot force grains to move with strains very close together when the γ' phase is harder plastically. Once the γ' is easier to deform with multiple modes operating, the two phases can co-deform more easily.

4.5. Model comparison with elastic strains in γ and γ'

The mean phase strains predicted by the model are shown in Fig. 8, in comparison with the experimental data already plotted in Fig. 3. Agreement for the 400 °C and 500 °C data sets is good. The capture of the initial yield in the γ' phase, followed by hardening and load transfer back towards the γ phase is correct, although the degree of this reverse load transfer is insufficient to cause the second crossover observed in the 500 °C data – at least at the strain applied. The agreement with the room temperature data is only qualitative. The softer response of the γ' phase is predicted, but significantly larger load transfer is predicted between the two phases than is actually observed. In contrast, the agreement between the model predictions and the 650 °C data set is excellent (similarly for 750 °C, not shown). However, the ability to match phase strains is only one feature of the model since – for example – the shift in which phase yields first must be chosen in order to match experimental data. For greater insight, we must compare the model predictions with the observed single peak strains.

4.6. Model comparison with single peak strains

The level of agreement observed in the phase average strains discussed above is comparable to that seen in the

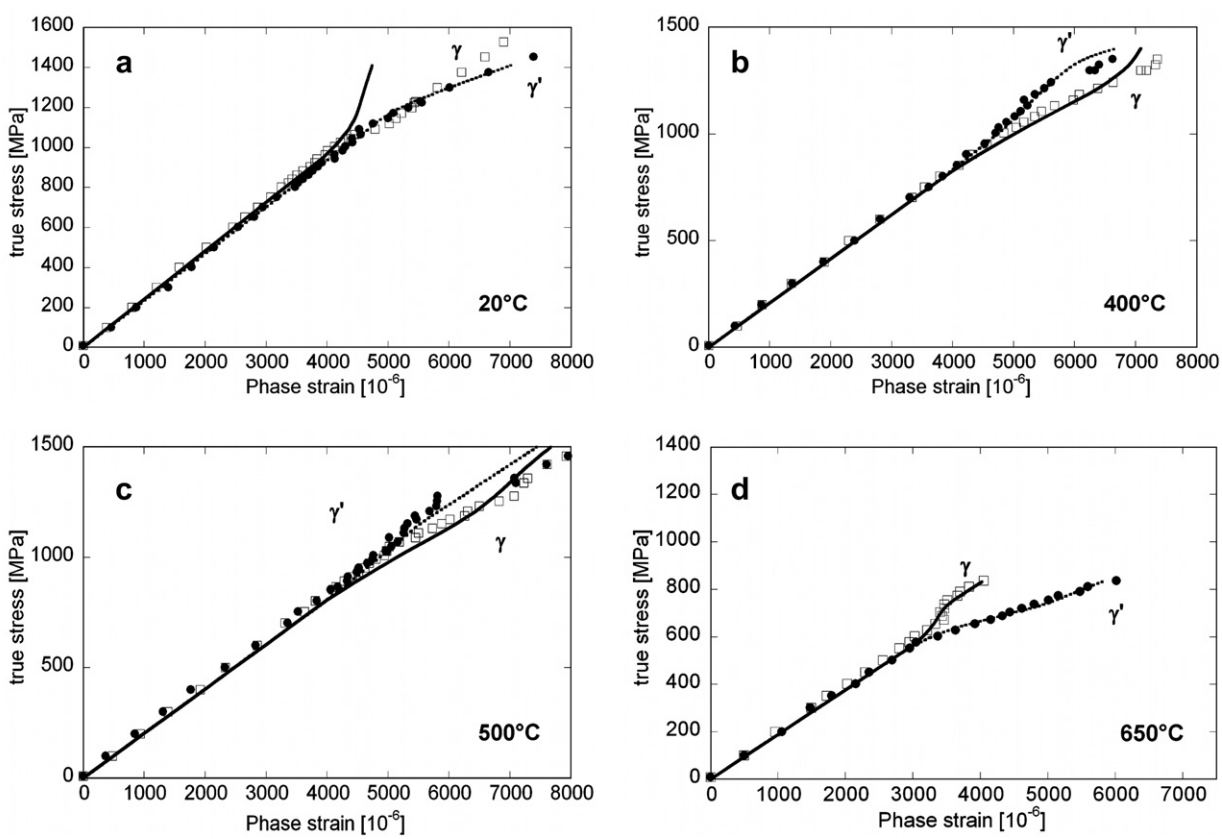

Fig. 8. Comparison of the axial elastic strain response of γ and γ' with EPSC predictions of the phases response during loading at (a) 20 °C, (b) 400 °C, (c) 500 °C, (d) 650 °C. Points are experimental data, while the lines represent model predictions.

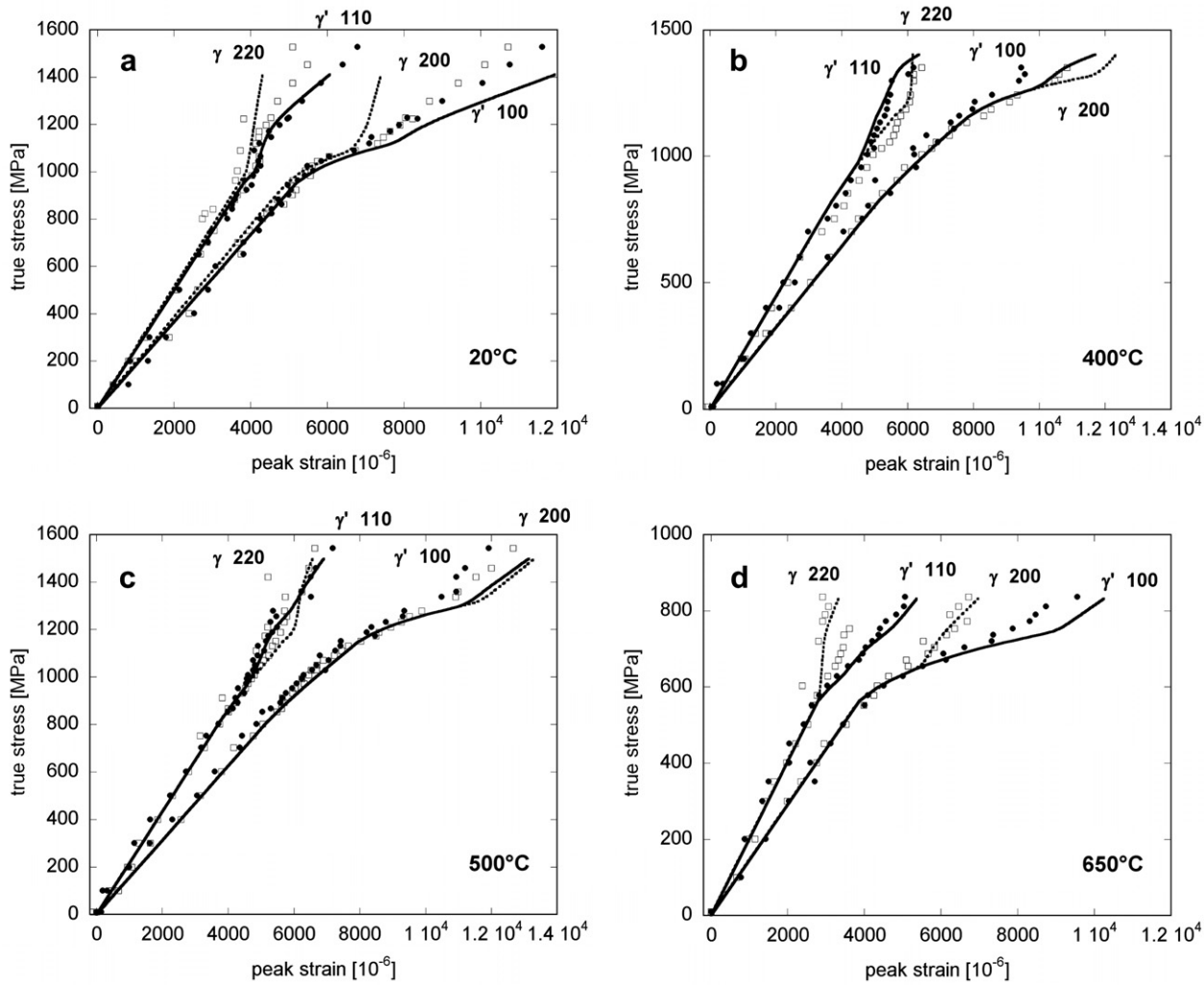

Fig. 9. Comparison of the axial elastic strain response of the (1 0 0) and (1 1 0) γ' superlattice reflections and the (2 0 0) and (2 2 0) γ reflections with EPSC predictions of the strain response of these grain/precipitate families during loading at (a) 20 °C, (b) 400 °C, (c) 500 °C, (d) 650 °C. Points are experimental data, while the lines represent model predictions.

doublet peak strains (Fig. 9a–d); however careful examination can provide additional information. First we note that the elastic anisotropy of the two phases is almost identical and is well captured with the elastic constants used. Secondly, if we consider the room temperature data in the plastic regime, we can see that there is an initial departure from linearity from the elastic response between 1000 MPa and 1100 MPa which is captured correctly by the model. It is only at the second inflection at around 1100 MPa that there are significant discrepancies between the model predictions and experiment – namely that the model predicts a much larger separation between the γ' and γ peak strains than is observed.

The data at 400 °C and 500 °C show reasonable agreement although there is some disagreement between model and experiment in the applied stress at which the second inflection in the (1 0 0) peaks occurs. This leads to discrepancies between the data and model for higher stresses, although the slope (hardening) is reasonably well captured. The agreement at 650 °C is excellent, although there is some failure to capture the second inflection in the γ' (1 0 0) response.

Perhaps the most interesting comparison between model and single peak strain data is seen however when we consider just the γ' peaks. In this phase we expect, and have modelled, a change in the slip systems, from pure $\langle 1\,1\,0\rangle\{1\,1\,1\}$ at room temperature to pure $\langle 1\,1\,0\rangle\{0\,0\,1\}$ at 750 °C, with the relative contributions changing as the temperature is raised. Fig. 10a–e shows the comparison between model and experiment; agreement is qualitatively excellent and quantitatively good. The elastic anisotropy and majority of inflections arising in the plastic zone are captured. Most significantly we see a clear shift in behaviour as temperature is raised; at low temperatures the plastic anisotropy of the (2 1 0) peak is only slightly different from that of the (1 1 0) peak, while the (1 0 0) peak is significantly different. At very high temperatures and at larger macroscopic plastic strains, the elastic strain of the (2 1 0)

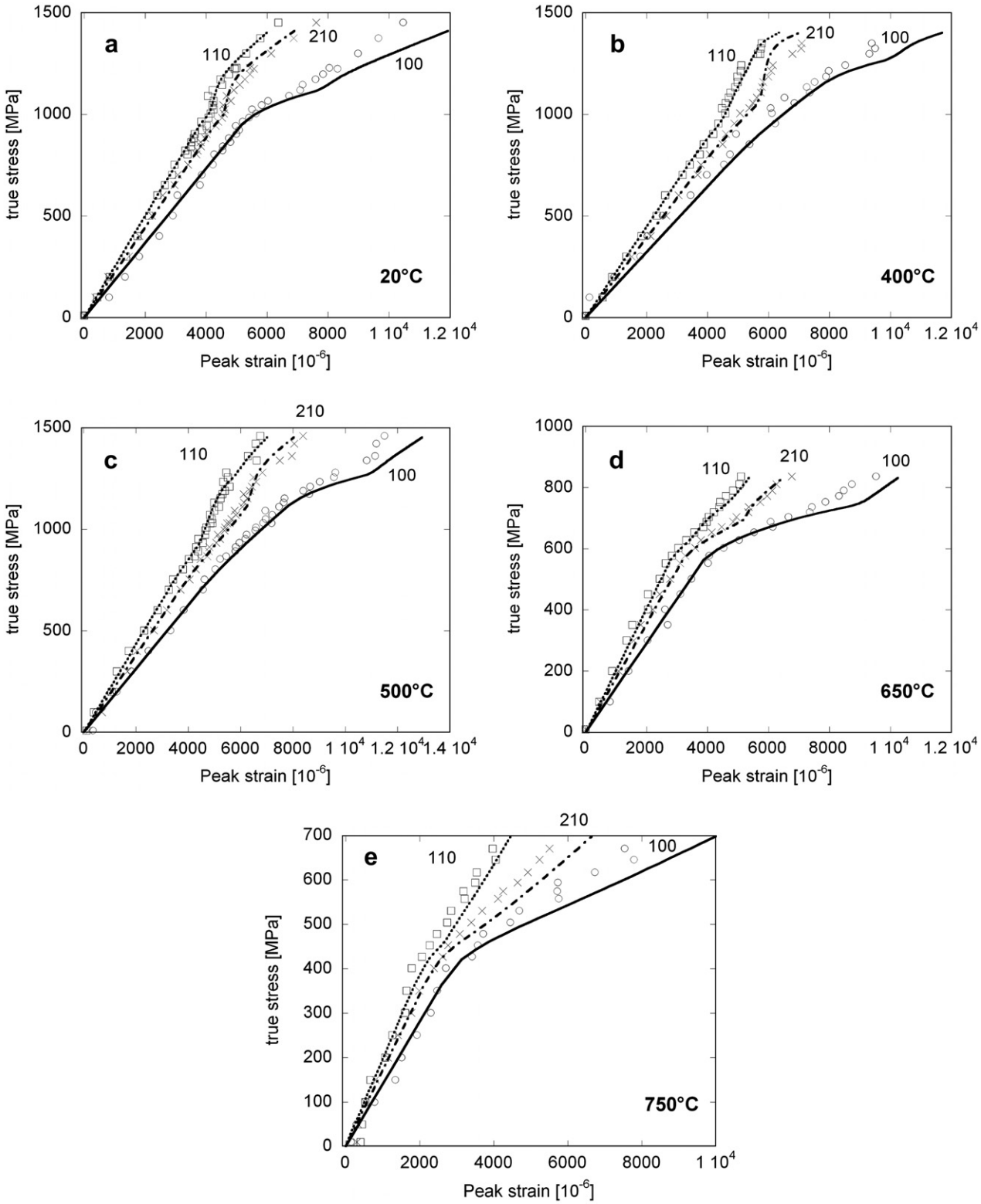

Fig. 10. Comparison of the axial elastic strain response the (100), (110) and (210) γ' superlattice reflections with EPSC predictions of the strain response of these precipitate families during loading at (a) 20 °C, (b) 400 °C, (c) 500 °C, (d) 650 °C and (e) 750 °C. Points are experimental data, while the lines represent model predictions.

peak sits roughly halfway between the strains observed in the (110) and (100) peaks. Based on the model predictions, this is a clear signature of the shift in operating slip mechanism from {111} towards {100} in the γ' phase of polycrystalline nickel-base superalloys as the temperature is increased.

5. Conclusions

A series of in situ loading experiments have been carried out on Alloy 720Li, an advanced polycrystalline nickel-base superalloy containing about 45 vol.% γ' at a range of temperatures, using the ENGIN-X neutron diffractometer at ISIS. The elastic strain response during elastic and plastic yielding of the material was captured for each phase (γ and γ') as well as for individual grain families. The strain results have been compared with the predictions of a self-consistent model to examine the changes in interphase and intergranular strains as a function of temperature. The model is in good agreement with the experimental predictions at elevated temperatures, but has only qualitative agreement at room temperature. It could be observed that at room temperature, 400 °C and 500 °C γ' represents the initially softer phase as the load is transferred to the γ phase during the onset of yielding. At these temperatures significant hardening occurs in the γ' phase during yielding and as plasticity progresses load is transferred back in the opposite direction. Instantaneous plastic yielding was observed at 400 °C and 500 °C after about 1.5% strain and at stress levels of about 1250 MPa, which coincides with zero misfit between γ and γ' in the axial direction.

At 650 °C and 750 °C the reverse load transfer is observed with the load being transferred to the γ' phase during the early stages of yielding. The variation of the elastic strain response of individual superlattice diffraction peaks of the γ' phase at different temperatures provided a clear signature, which could be correlated with the change in operating slip mechanism from {111} to {100} with increasing temperature. This change of slip mode is well documented in the literature for single crystal nickel-base superalloys and was experimentally verified by transmission electron microscopy studies [13]. The present work demonstrates that the change of slip mode can be detected in situ in bulk polycrystalline material when undertaking in situ loading on an advanced neutron diffraction beam line such as ENGIN-X.

Acknowledgements

The experimental programme benefited from the use of the ISIS Facility at the Rutherford Appleton Laboratory, UK and material supply from Rolls Royce plc. The authors would also like to thank Professor T. Mori for many fruitful discussions.

Appendix A.

In the following; ε^i, α^i and L^i are the strain increment, thermal factor and stiffness tensors for inclusion i, respectively. For the two-site model $i = 1,2$. E^0, A^0 and L^0 are the overall strain increment, thermal factor and stiffness tensors, respectively. Γ^{ij} are the four Green's function tensors, see the appendix of Ref. [38]. $\Delta T$is the temperature increment and δL^i is the stiffness difference ($\delta L^i = L^i - L^0$) for inclusion i. $\varepsilon^*$is the uniform effective eigen-strain for the two-site problem. The strain in each inclusion can be found as

$$\begin{aligned}\varepsilon^1 &= \varepsilon^* + \Gamma^{11} : [\delta L^1 : \varepsilon^1 - L^1 : \alpha^1 \Delta T] + \Gamma^{12} : [\delta L^2 : \varepsilon^2 - L^2 : \alpha^2 \Delta T] \\ \varepsilon^2 &= \varepsilon^* + \Gamma^{21} : [\delta L^1 : \varepsilon^1 - L^1 : \alpha^1 \Delta T] + \Gamma^{22} : [\delta L^2 : \varepsilon^2 - L^2 : \alpha^2 \Delta T]\end{aligned} \tag{A1}$$

By rearranging these equations in block form we find

$$\begin{aligned}A^{11} : \varepsilon^1 + A^{12} : \varepsilon^2 &= \varepsilon^* - V^1 \\ A^{21} : \varepsilon^1 + A^{22} : \varepsilon^2 &= \varepsilon^* - V^2\end{aligned} \tag{A2}$$

where

$$\begin{aligned}&A^{11} = I - \Gamma^{11} : \delta L^1, \quad A^{22} = I - \Gamma^{22} : \delta L^2 \\ &A^{12} = -\Gamma^{12} \delta L^2, \quad A^{21} = -\Gamma^{21} \delta L^1 \\ &V^1 = \Gamma^{11} : L^1 : \alpha^1 \Delta T + \Gamma^{12} : L^2 : \alpha^2 \Delta T, \\ &V^2 = \Gamma^{21} : L^1 : \alpha^1 \Delta T + \Gamma^{22} : L^2 : \alpha^2 \Delta T\end{aligned} \tag{A3}$$

By isolating the strain components ε^1 and ε^2 in Eq. (A2) we find that

$$\begin{aligned}\varepsilon^1 &= \Lambda^1 : \varepsilon^* - \tilde{\varepsilon}^1 \\ \varepsilon^2 &= \Lambda^2 : \varepsilon^* - \tilde{\varepsilon}^2\end{aligned} \tag{A4}$$

where

$$\begin{aligned}\Lambda^1 &= [A^{11} - A^{12} : [A^{22}]^{-1} : A^{21}]^{-1} : [I - A^{12} : [A^{22}]^{-1}] \\ \Lambda^2 &= [A^{22} - A^{21} : [A^{11}]^{-1} : A^{12}]^{-1} : [I - A^{21} : [A^{11}]^{-1}] \\ \tilde{\varepsilon}^1 &= [A^{11} - A^{12} : [A^{22}]^{-1} : A^{21}]^{-1} : [V^1 - A^{12} : [A^{22}]^{-1} : V^2] \\ \tilde{\varepsilon}^2 &= [A^{22} - A^{21} : [A^{11}]^{-1} : A^{12}]^{-1} : [V^2 - A^{21} : [A^{11}]^{-1} : V^1]\end{aligned} \tag{A5}$$

The overall strain increment is found as the average of the strain increments in the inclusions (no superscript is used under the $\langle \cdots \rangle$ signs, as the averages are taken over both inclusions)

$$E^0 = \langle \varepsilon \rangle = \langle \Lambda \rangle : \varepsilon^* - \langle \tilde{\varepsilon} \rangle \tag{A6}$$

and thereby the uniform effective eigen-strain is found as

$$\varepsilon^* = \langle \Lambda \rangle^{-1} : [E^0 + \langle \tilde{\varepsilon} \rangle] \tag{A7}$$

The stresses in the inclusions are given by

$$\begin{aligned}\sigma^1 &= L^1 : [\varepsilon^1 - \alpha^1 \Delta T] \\ \sigma^2 &= L^2 : [\varepsilon^2 - \alpha^2 \Delta T]\end{aligned} \tag{A8}$$

and by combining the above equations we find that

$$\begin{aligned}\sigma^1 &= L^1 : [\Lambda^1 : \langle \Lambda \rangle^{-1} : [E^0 + \langle \tilde{\varepsilon} \rangle] - \tilde{\varepsilon}^1 - \alpha^1 \Delta T] \\ \sigma^2 &= L^2 : [\Lambda^2 : \langle \Lambda \rangle^{-1} : [E^0 + \langle \tilde{\varepsilon} \rangle] - \tilde{\varepsilon}^2 - \alpha^2 \Delta T]\end{aligned} \tag{A9}$$

The overall stress is then found as

$$\begin{aligned}S^0 &= L^0 : [E^0 - A^0 \Delta T] \\ &= \langle \sigma \rangle = \langle L : \Lambda \rangle : \langle \Lambda \rangle^{-1} : [E^0 + \langle \tilde{\varepsilon} \rangle] - \langle L : [\tilde{\varepsilon} + \alpha \Delta T] \rangle\end{aligned} \tag{A10}$$

Thereby the overall stiffness, L^0, is found as

$$L^0 = \langle L : \Lambda \rangle : \langle \Lambda \rangle^{-1}$$

and the overall thermal parameter, A^0, is found as

$$A^0 = \frac{[L^0]^{-1} : \langle L : [\tilde{\varepsilon} + \alpha \Delta T] \rangle - \langle \tilde{\varepsilon} \rangle}{\Delta T} \tag{A11}$$

References

[1] Sims CT, Stolokoff NS, Hagel WC. Superalloys II. New York: John Wiley & Sons; 1987.
[2] Reppich B. Acta Metall 1982;30(1):87–94.
[3] Reppich B, Schepp P, Wehner G. Acta Metall 1982;30(1):95–104.
[4] Maniar GN. Metall Trans 1970;1:31–42.
[5] Reppich B, Kühlein W, Meyer G, Puppel D, Schulz M, Schumann G. Mater Sci Eng 1986;83(1):45–63.
[6] Westbrook JH. Trans TMS-AIME 1957;209:898–904.
[7] Thornton PH, Davies RG, Johnston TL. Met Trans 1970;1:207–18.
[8] Staton-Bevan AE, Rawlings RD. Phys Status Solidi (a) 1975;29:613–22.
[9] Kohler JS, Seitz F. J Appl Mech 1947;14:A217–24.
[10] Taunt RJ, Ralph B. Philos Mag 1974;30:1379–94.
[11] Lall C, Chin S, Pope DP. Metall Trans A 1979;10A:1323–32.
[12] Shah D, Lin L. J Met 1980;32(8):62.
[13] Clement N, Couret A, Caillard D. Philos Mag A 1991;64:669–94.
[14] Decker RF, Mihalisin JR. Trans ASM 1969;62(2):481.
[15] Hutchings MT, Withers PJ, Holden TM, Lorentzen T. Introduction to the characterization of residual stress by neutron diffraction, 401. Boca Raton, FL: Taylor & Francis; 2005.
[16] Noyan IC, Cohen JB. Residual stress – measurement by diffraction and interpretation. In: Ilschner B, Grant NJ, editors. Materials research and engineering, 272. New York: Springer-Verlag; 1987.
[17] Fitzpatrick ME, Lodini A, editors. Analysis of residual stress by diffraction using neutron and synchrotron diffraction, 348. London: Taylor & Francis; 2003.
[18] Santisteban JR, Daymond MR, James JA, Edwards L. J Appl Cryst 2006;39:812–25.
[19] Daymond MR, Priesmeyer HG. Acta Mater 2002;50(6):1613–26.
[20] Daymond MR, Withers PJ. Scripta Mater 1996;35(6):717–20.
[21] Windsor CG. Pulsed neutron scattering. London: Taylor & Francis; 1981.
[22] Rietveld HM. J Appl Cryst 1969;2:65–71.
[23] Larson AC, Von Dreele RB. GSAS – General structure analysis system. Los Alamos National Laboratory; 1994.
[24] Von Dreele RB, Jorgensen JD, Windsor CG. J Appl Cryst 1982;15:581–9.
[25] Stone HJ, Holden TM, Reed RC. Acta Mater 1999;47(17):4435–48.
[26] Ma S, Rangaswamy P, Majumdar BS. Scripta Mater 2003; 48(5):525–30.
[27] Ma S, Brown D, Bourke MAM, Daymond MR, Majurndar BS. Mater Sci Eng A 2005;399(1–2):141–53.
[28] Akeroyd FA, Ashworth RL, Johnston SD, Martin JM, Moreton-Smith CM, Sivia DS. OpenGenie 1999.
[29] Miller RF, Ansell GS. Metall Trans 1977;8(12):1979–91.
[30] Hill R. J Mech Phys Sol 1965;13:89–101.
[31] Hutchinson JW. Proc Roy Soc London A 1970;319:247–72.
[32] Eshelby JD. Proc Roy Soc London A 1959;252:561–9.
[33] Turner PA, Christodoulou N, Tomé CN. Int J Plast 1995;11(3):251–65.
[34] Clausen B, Lorentzen T, Bourke MAM, Daymond MR. Mater Sci Eng A 1999;259(1):17–24.
[35] Daymond MR, Bonner NW. Mater Sci Eng A 2002;340:263–71.
[36] Daymond MR, Hartig C, Mecking H. Acta Mater 2005;53(9):2805–13.
[37] Daymond MR, Fitzpatrick ME. Met Mater Trans A 2006;37A:1977–86.
[38] Lebensohn RA, Canova GR. Acta Mater 1997;45(9):3687–94.
[39] Canova GR. Private communication.
[40] Prikhodko SV, Carnes JD, Isaak DG, Yang H, Ardell AJ. Met Mater Trans A 1999;30A:2403–8.
[41] Cho JR, Dye D, Conlon KT, Daymond MR, Reed RC. Acta Mater 2002;50(19):4847–64.
[42] Dye D, Stone HJ, Reed RC. Acta Mater 2001;49(7):1271–83.
[43] Kocks UF, Tomé CN, Wenk H-R. Texture and anisotropy. Cambridge: Cambridge University Press; 1998.
[44] Kocks UF, Mecking H. Prog Mater Sci 2003;48:171–3.
[45] Nembach E. Mater Sci Eng A 2006;429:277–86.
[46] Daymond MR, Bourke MAM, Von Dreele RB, Clausen B, Lorentzen T. J Appl Phys 1997;82(4):1554–62.
[47] Daymond MR. J Appl Phys 2004;96(8):4263–72.
[48] Van Acker K, Root JH, Houtte PV, Aernoudt E. Acta Mater 1996;44(10):4039–49.
[49] Preuss M, Withers PJ, Maire E, Buffiere J-Y. Acta Mater 2002;50(12):3177–92.